Journal of Current Science and Technology, April-June 2026 Vol. 16 No. 2, Article 176

ISSN 2630-0656 (Online)

Cite this article: Keawchaloon, A., Phatungthane, T., Prasomthong, S., & Chomchalao, C. (2026). Artificial neural network–genetic algorithm integrated approach for optimizing residual stress and crystallite size in incremental forming of Ti–6Al–4V alloy. *Journal of Current Science and Technology*, *16*(2), Article 176. https://doi.org/10.59796/jcst.V16N2.2026.176

Journal of Current Science and Technology

Journal homepage: https://jcst.rsu.ac.th

Artificial Neural Network–Genetic Algorithm Integrated Approach for Optimizing Residual Stress and Crystallite Size in Incremental Forming of Ti–6Al–4V Alloy

Apisit Keawchaloon[1], Thanatep Phatungthane[2], Suriya Prasomthong[1] and Chaiya Chomchalao[1,*]

[1]Department of Industrial Technology, Nakhon Phanom University, Nakhon Phanom 48000, Thailand
[2]Division of Science, Faculty of Education, Nakhon Phanom University, Nakhon Phanom 48000, Thailand

[*]Corresponding author; E-mail: chaiwelding@ms.npu.ac.th

Received 1 October 2025; Revised 10 November 2025; Accepted 27 November 2025; Published online 30 March 2026

Abstract

This study develops an integrated Artificial Neural Network–Genetic Algorithm (ANN–GA) approach to optimize process parameters in incremental sheet forming (ISF) of Ti–6Al–4V alloy, aiming to minimize residual stress (RS) and maximize crystallite size (D) to improve product quality. Three parameters tool radius (R), incremental step depth (S), and feed rate (F) were arranged using a Taguchi L9 orthogonal array. An ANN model (3–5–2 architecture), trained with the Levenberg–Marquardt algorithm, predicted RS and D, while GA was employed to determine optimal parameter combinations for simultaneous multi-response optimization. Experimental results showed RS between −157.11 MPa and −86.99 MPa and D from 19.67 to 21.87 nm. The ANN–GA method achieved superior prediction accuracy. The ANN model achieved a training RMSE of 0.0301 MPa for RS and 0.1394 nm for D, whereas validation RMSE values were 1.842 MPa and 0.229 nm, respectively, confirming good generalization performance. The optimal settings (R = 8.725 mm, S = 0.2588 mm, F = 1 mm·min^{-1}) reduced the magnitude of residual stress by 9.18% and increased D by 5.27% compared with the best Taguchi results. This integrated framework enhances process reliability, enables precise control of surface integrity, and provides practical guidelines for manufacturing high-performance titanium components for aerospace and biomedical applications.

Keywords: *incremental sheet forming; Ti–6Al–4V; Artificial Neural Network (ANN); Genetic Algorithm (GA); residual stress; crystallite size*

1. Introduction

Incremental Sheet Forming (ISF) has gained attention for its flexibility and low tooling cost, making it particularly suitable for prototyping and small-batch production of sheet metal components. However, ISF inherently induces non-uniform deformation and localized strain, which can lead to elevated residual stresses and crystallite refinement, thereby affecting dimensional stability and structural integrity. While previous studies have examined the effects of step depth, feed rate, and tool geometry on formability and surface quality (Kumar et al., 2021), the specific influence of tool diameter on microstructural evolution in Ti–6Al–4V alloys remains underexplored.

ISF, including single-point incremental forming (SPIF), incrementally deforms a sheet without the need for dies, offering advantages for difficult-to-form materials such as titanium alloys that are widely used in aerospace and biomedical applications (Oleksik et al., 2021). The process produces localized plastic deformation, which can generate microstrain, induce phase transformations, and reduce crystallite size (Oleksik et al., 2021). Although approaches such as elevated temperature and lubrication have been employed to improve formability and surface integrity (Ortiz et al., 2019), systematic studies examining the role of tool diameter in modifying stress distribution and

microstructural responses through X-ray diffraction (XRD) analysis remain limited.

Recent reviews and experiments have addressed ISF process mechanics, parameter influences, and surface quality (Popp et al., 2024), with some investigations focusing on residual stress (Kajal et al., 2023). Yet, there is a lack of targeted, quantitative research linking tool diameter to microstructural evolution in Ti–6Al–4V, particularly through XRD and Williamson–Hall analysis for evaluating crystallite size and microstrain. The combined effects of tool diameter, step depth, and feed rate on residual stress and crystallite refinement are not fully understood, restricting process optimization strategies. Previous ISF studies reported residual stress fluctuations of 40–120 MPa in Ti–6Al–4V components, with crystallite size variation up to 8–15%, yet no study quantitatively linked these variations to tool radius or combined parameter effects.

To address this gap, the present study systematically investigates the effects of tool diameters (6 mm, 8 mm, and 10 mm), along with variations in step depth and feed rate, on the microstructural behavior of Ti–6Al–4V during ISF. Using XRD and Williamson–Hall analysis, the study quantifies relationships among tool diameter, lattice strain, and crystallite size. Results reveal that larger tool diameters reduce microstrain and enlarge crystallite domains, contributing to improved dimensional stability and structural integrity. By consolidating prior findings on ISF mechanics and parameter effects (Oleksik et al., 2021; Ortiz et al., 2019; Kumar et al., 2021; Kajal et al., 2023; Coman et al., 2023; Murugesan et al., 2022; Popp et al., 2024), this work provides new insights into microstructural control and practical guidelines for parameter optimization in producing high-performance titanium components. Ti–6Al–4V exhibits low room-temperature ductility, high yield strength, and poor strain accommodation, making it highly sensitive to forming parameters. These characteristics lead to severe strain localization, significant lattice distortion, and high compressive residual stresses during incremental forming. Thus, optimization is essential to achieve precise microstructural control.

Despite substantial progress in understanding ISF mechanics, the combined effect of tool radius, step depth, and feed rate on the microstructural response of Ti–6Al–4V remains insufficiently addressed. Therefore, the present study integrates experimental XRD analysis with AI-based optimization to close this gap. Therefore, this study aims to clarify the influence of tool diameter in combination with step depth and feed rate on the residual stress and crystallite size in Ti–6Al–4V alloy during incremental sheet forming. By integrating X-ray diffraction analysis with advanced modeling and optimization techniques, the research seeks to provide quantitative insights into process–microstructure relationships. These findings are expected to establish practical guidelines for optimizing forming parameters to enhance the structural integrity and dimensional stability of titanium components.

2. Objectives

The objective of this study is to examine how key process parameters in incremental sheet forming, namely tool radius, step depth, and feed rate, affect the residual stress and crystallite size of Ti–6Al–4V alloy. X-ray diffraction and Williamson–Hall analysis are employed to establish quantitative relationships between processing conditions and microstructural evolution. To achieve this, an Artificial Neural Network integrated with a Genetic Algorithm is applied to optimize multiple responses, aiming to minimize residual stress while maximizing crystallite size to enhance structural integrity and process reliability.

3. Materials and Methods

3.1 Material

The material used in this incremental forming experiment was Grade 5 titanium alloy (Ti–6Al–4V) with a nominal thickness of 0.5 mm. The certified chemical composition provided by the manufacturer is presented in Table 1, showing Ti as the balance with 6.2 wt.% Al, 4.0 wt.% V, and minor elements such as Fe, O, C, and N. Mechanical characterization was conducted using X-ray diffraction (XRD) to determine crystallite size (D), microstrain (ε), and residual stress (σ). Measurements were based on the full width at half maximum (FWHM) method, analyzing peak broadening of indexed planes using Williamson–Hall plots, as shown in Figure 1(a) and (b). The results, summarized in Table 2, indicate a crystallite size of 51.62 nm, a microstrain of -4.60×10^{-4}, and a compressive residual stress of −56.49 MPa, with an elastic modulus (E) of 114.8 GPa and a Poisson's ratio (ν) of 0.322. The forming tool was manufactured from SKD-11 tool steel due to its high hardness and wear resistance, ensuring dimensional stability during forming operations. From a crystallographic perspective, Ti–6Al–4V exhibits a dual-phase α+β microstructure, where the α-phase (hexagonal close-packed, HCP) provides strength and creep resistance, while the β-phase (body-centered cubic, BCC) improves ductility. This balance makes Ti–6Al–4V an ideal candidate for precision incremental forming in advanced manufacturing.

Table 1 Certified Nominal Chemical Composition of Ti–6Al–4V Alloy (in weight percent)

Material	Chemical composition (%wt)						
	Ti	Al	V	Fe	O	N	Other
Ti–6Al–4V	Bal.	6.2	4	0.2	0.1	0.01	0.5

Table 2 XRD-Derived Mechanical Properties of Ti–6Al–4V Alloy

Material	Mechanical Properties				
	Crystallite size; D (nm)	Microstrain (ε) (x 10^{-4})	Residual stress(σ) (MPa)	E (GPa)	*v*
Ti–6Al–4V	51.62	–4.60	–56.49	114.8	0.322

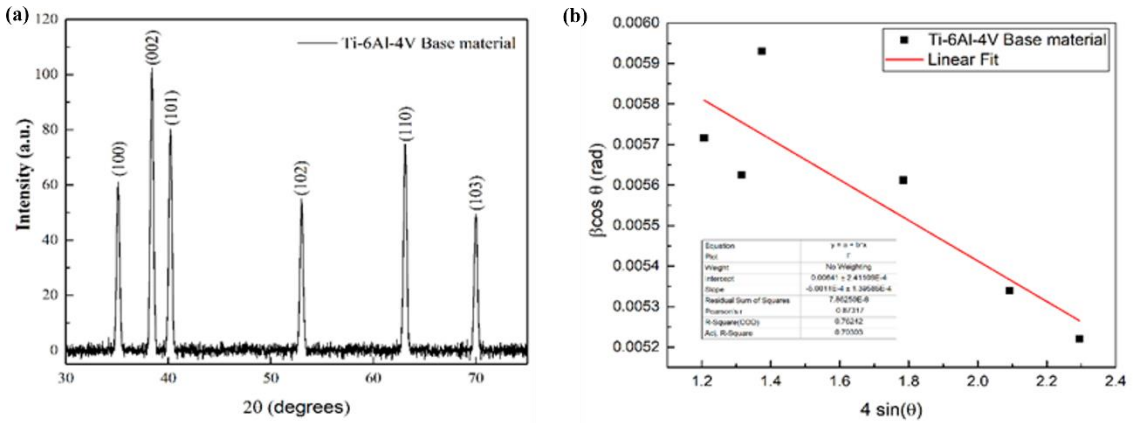

Figure 1 (a) XRD pattern and (b) Williamson–Hall plot of Ti–6Al–4V base material prior to incremental forming.

3.2 Incremental Setup and XRD Analysis

The experimental setup and X-ray diffraction (XRD) analysis procedure are illustrated in Figure 2. The Ti–6 Al–4 V sheets were sourced from Metals World Store (China), with material specifications provided by the supplier in accordance with American Society for Testing and Materials standards. Each forming condition in the L9 array was conducted once, resulting in 9 experimental samples. The Taguchi L9 design was employed to efficiently explore the effects of process parameters with a minimal number of experiments. However, no replicates were included (n = 1 per run), and this is acknowledged as a limitation of the study. Future work should incorporate repeated trials to improve statistical robustness and enable uncertainty analysis.

A two-point incremental forming (TPIF) configuration was employed, in which the forming tool was mounted on a computer numerical control spindle, and the Ti–6 Al–4 V sheet was securely clamped on the fixture with a partial die positioned beneath the workpiece, as shown in Figure 2(a). A Superlene nylon partial die was used to provide localized support during the forming process, as presented in Figure 2(b). The schematic of the forming process in Figure 2(c) shows the tool profile, tool radii of 6, 8, and 10 mm, step depths of 0.2, 0.3, and 0.4 mm, and feed rates of 0.50, 0.75, and 1.00 mm·min^{-1}. A cross-sectional view of the deformation region is also indicated in Section A–A, together with the spiral tool path.

The formed Ti–6 Al–4 V workpiece, with the precise location of specimen extraction for XRD analysis, is shown in Figure 2(d). Square specimens with dimensions of 10 mm × 10 mm were sectioned from the central deformation zone to ensure representative measurements. The XRD measurement schematic is illustrated in Figure 2(e), where Cu Kα radiation (λ = 1.5406 Å) was employed over a 2θ range of 25°–80° with a step size of 0.02°. Peak positions and full width at half maximum (FWHM) values were fitted using a Gaussian profile. Crystallite size (D) was calculated using the Scherrer equation (k = 0.9), and residual stress (σ) was evaluated using Williamson–Hall (W–H) plots, enabling accurate characterization of the microstructural state of the formed alloy.

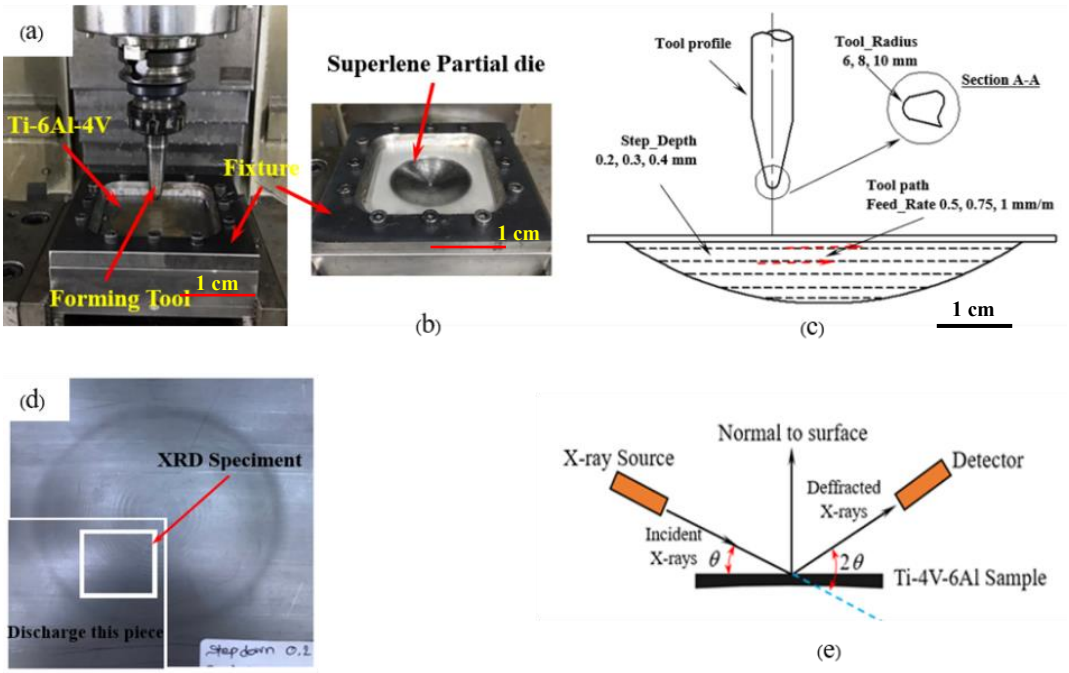

Figure 2 Schematic representation of the experimental setup, process parameters, and XRD specimen preparation in incremental sheet forming of Ti–6Al–4V alloy

3.3 Williamson–Hall Analysis

To determine both crystallite size (D) and residual stress (σ) in the incrementally formed Ti–6Al–4V sheets, the Williamson–Hall (W–H) method was applied to the X-ray diffraction (XRD) data. The Williamson–Hall method was selected because it simultaneously separates crystallite size effects and microstrain broadening, requires fewer assumptions than the Warren–Averbach method, and avoids the noise sensitivity of Halder–Wagner analysis, making it suitable for titanium alloys with mixed α+β phases. This technique separates peak broadening contributions arising from finite crystallite size and lattice strain, enabling the simultaneous estimation of coherent domain size and microstrain (ε) using a simple linear fitting procedure. The major reflections corresponding to the α and β phases were identified from the diffractograms, and their peak positions (2θ) and full width at half maximum (FWHM, β) values were extracted using constrained Gaussian fitting. Instrumental broadening was subtracted using a standard reference material to obtain physical broadening. All angles and peak widths were converted to radians prior to analysis.

The basic Williamson– Hall relation used in this work is expressed as Equation (1).

$$\beta\cos\theta = \frac{k\lambda}{D} + 4\varepsilon\sin\theta \quad (1)$$

where β is the FWHM in radians, θ is the Bragg diffraction angle (in radians) , D is the effective crystallite size in nanometers, ε is the microstrain (dimensionless) , k is the shape factor (taken as 0. 9) , and λ is the X-ray wavelength (0.15406 nm for Cu Kα radiation) . For each diffraction peak i, the values $\beta_i\cos\theta_i$ and $4\sin\theta_i$ were calculated, and a least-squares regression was performed with $\beta\cos\theta$ as the ordinate and $4\sin\theta$ as the abscissa.

When residual stress evaluation was required, the Uniform Deformation Stress Model (UDSM) was adopted, which extends the W–H method. In Equation (2), {hkl} denotes the crystallographic plane family associated with the diffraction peak, which governs the anisotropic elastic response of Ti–6Al–4V.

$$\beta\cos\theta = \frac{k\lambda}{D} + \frac{4\sigma}{E_{hkl}}\sin\theta \quad (2)$$

Here, E_{hkl} is the diffraction elastic modulus for the {hkl} reflection, accounting for the crystallographic anisotropy of Ti–6Al–4V.

Residual stress was then obtained from microstrain using Hooke' s law for elastic lattice deformation.

$$\sigma = E_{iso}\varepsilon \quad (3)$$

In Equation (3), the elastic modulus is expressed as the isotropic Young's modulus (E_{iso} = 114.8 GPa), which differs from the orientation-dependent modulus (E_{hkl}) defined in Equation (2). A negative σ denotes compressive residual stress, while a positive value indicates tensile stress. The robustness of the fit was verified using the coefficient of determination (R^2) and leave-one-peak-out sensitivity checks. The leave-one-peak-out sensitivity test evaluates the stability of fitted microstrain by removing one diffraction peak at a time and re-fitting the W–H line; a large deviation indicates that the removed peak is unreliable or affected by texture. Peaks affected by overlap, preferred orientation, or low signal-to-noise ratio were down-weighted or excluded from the regression to minimize bias. This approach provides a reliable and reproducible link between ISF process parameters (tool radius, step depth, and feed rate) and the resulting microstructural refinement (via D) and lattice stress state (via σ) in Ti–6Al–4V components.

3.4 Prediction and Optimization

3.4.1 Taguchi Experimental Design

The Taguchi method was employed using an L9 orthogonal array to efficiently investigate the effects of three process parameters—tool radius (R), incremental step depth (S), and feed rate (F)—each at three levels, while minimizing the number of required experiments. The selected parameter levels are summarized in Table 3, which presents the factor values determined based on prior literature and preliminary trials to ensure their relevance to incremental sheet forming (ISF) of Ti–6Al–4V. It should be noted that each experimental condition was conducted once (n = 1), and therefore, the results primarily provide a comparative assessment of parameter effects rather than a statistically replicated analysis.

The experimental plan was structured according to the L9 orthogonal array shown in Table 4 (Charonerat et al., 2025), ensuring that all possible factor combinations were represented in a balanced manner while avoiding unnecessary repetition. The quality metric for residual stress (RS) was evaluated using the smaller-is-better criterion (Equation 4), as lower RS is desirable to reduce the risks of dimensional instability, springback, fatigue crack initiation, and non-uniform stress distribution in thin-sheet ISF. Conversely, crystallite size (D) was evaluated using the larger-is-better criterion (Equation 5), since a larger coherent domain size generally indicates reduced lattice distortion and improved post-forming structural stability, which aligns with the dimensional accuracy and integrity objectives of this study.

$$S/N_{smaller} = -10\log_{10}\left(\frac{1}{n}\sum_{i=1}^{n} y_i^2\right) \tag{4}$$

$$S/N_{larger} = -10\log_{10}\left(\frac{1}{n}\sum_{i=1}^{n} \frac{1}{y_i^2}\right) \tag{5}$$

Table 3 Process parameters and factor levels for ISF experiments.

Parameter (symbol)	Level 1	Level 2	Level 3	Unit
Tool radius (R)	6	8	10	mm
Incremental step depth (S)	0.2	0.3	0.4	mm
Feed rate (F)	0.5	0.75	1	mm·min^{-1}

Table 4 Taguchi L9 orthogonal array for ISF of Ti–6Al–4V.

Run	Tool radius (R)	Incremental step depth (S)	Feed rate (F)
1	6	0.2	0.5
2	6	0.3	0.75
3	6	0.4	1
4	8	0.2	0.75
5	8	0.3	1
6	8	0.4	0.5
7	10	0.2	1
8	10	0.3	0.5
9	10	0.4	0.75

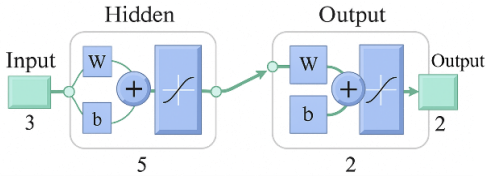

Figure 3 Architecture of the ANN model showing the data flow from input neurons through the hidden layer to output neurons

3.4.2 ANN Prediction Modeling

An Artificial Neural Network (ANN) model was developed to predict residual stress (RS) and crystallite size (D) from the key incremental sheet forming (ISF) process parameters: tool radius (R), incremental step depth (S), and feed rate (F). The network architecture, illustrated in Figure 3, consisted of three layers: an input layer with three neurons corresponding to R, S, and F; a hidden layer with five neurons employing a nonlinear activation function; and an output layer with two neurons corresponding to the predicted RS and D values.

The number of hidden neurons was determined through hyperparameter tuning across 3–10 neurons. The 5-neuron configuration produced the lowest RMSE while avoiding overfitting, as confirmed by early stopping validation.

Training was carried out using a feed-forward backpropagation algorithm governed by the Levenberg–Marquardt learning rule, with a learning rate of 0.5, a momentum constant of 0.4, and transfer function coefficients of 0.6, 1.4, and 0.6 for the input, hidden, and output layers, respectively. A bias value of 0.0005 was assigned to all layers. Prior to training, all input parameters were normalized using the min–max scaling method, expressed as:

$$\tilde{x}_j = \frac{x_j - x_{j,\min}}{x_{j,\max} - x_{j,\min}}, \quad j \in \{R, S, F\} \tag{6}$$

The transformation from the normalized input vector $\hat{x}$ to the output predictions $\hat{y}$ is expressed through the hidden layer activation (Equation 7) and the output layer computation (Equation 8):

$$a^{(1)} = \phi\left(W^{(1)}x + b^{(1)}\right), \quad y = W^{(2)}a^{(1)} + b^{(2)} \tag{7}$$

$$\text{MSE} = \frac{1}{N}\sum_{i=1}^{N}\left[(RS_i - RS_i)^2 + (D_i - \hat{D}_i)^2\right] \tag{8}$$

where N is the total number of experimental data samples, $W^{(1)}$ and $W^{(2)}$ are the weight matrices, $b^{(1)}$ and $b^{(2)}$ are bias vectors, and ϕ is the activation function.

3.4.3 ANN-GA Optimization

The trained ANN model served as a high–fidelity surrogate for the GA–based optimization process. The goal was to simultaneously minimize residual stress and maximize crystallite size, which were consolidated into a single weighted fitness function (Equation 9):

$$f(\mathbf{x}) = w_{RS}\frac{RS(\mathbf{x}) - RS_{\min}}{RS_{\max} - RS_{\min}} + w_D\frac{D_{\max} - \hat{D}(\mathbf{x})}{D_{\max} - D_{\min}}, \quad w_{RS} + w_D = 1 \tag{9}$$

To ensure the feasibility of the optimized solutions, a penalty function was introduced to handle violations of the process parameter constraints (Equation 10):

$$\tilde{f}(\mathbf{x}) = f(\mathbf{x}) + \rho\begin{bmatrix}\max(0, R - R_U)^2 + \max(0, R_L - R)^2 \\ +\max(0, S - S_U)^2 + \max(0, S_L - S)^2 \\ +\max(0, F - F_U)^2 + \max(0, F_L - F)^2\end{bmatrix} \tag{10}$$

Here, R_L, R_U, S_L, S_U, F_L, and F_U represent the lower and upper bounds of the respective process parameters, and ρ is the penalty coefficient.

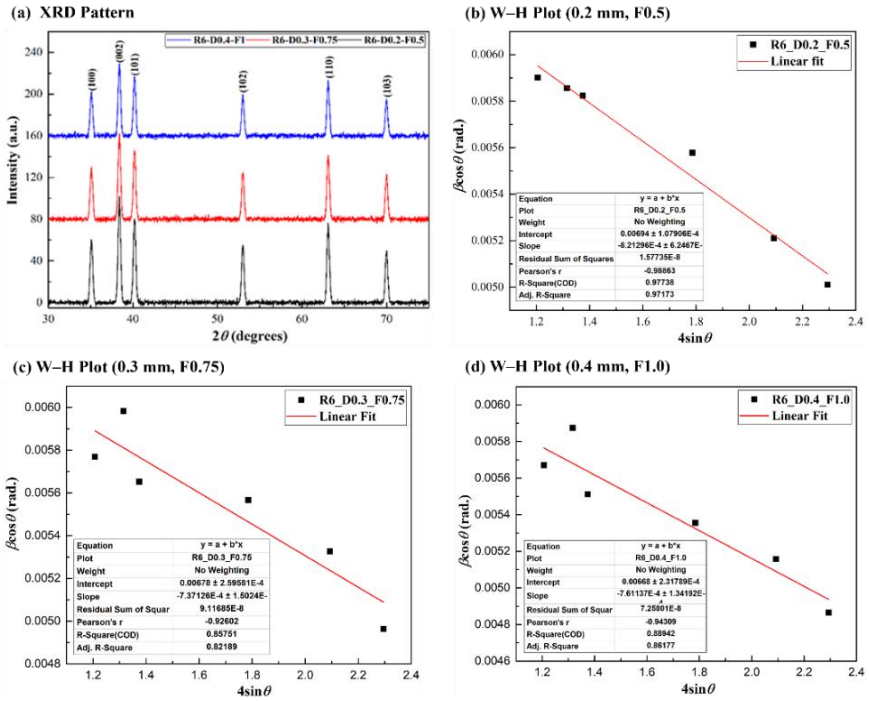

Figure 4 (a) XRD patterns of Ti–6Al–4V formed with a constant 6 mm tool diameter under varied step depths and feed rates. (b–d) Williamson–Hall plots for residual stress and crystallite size evaluation.

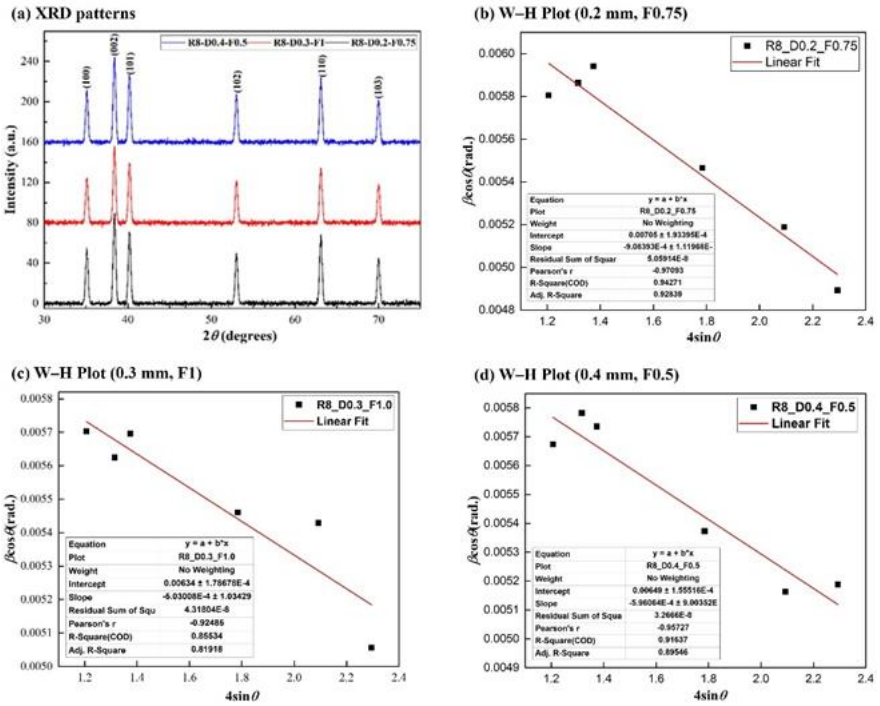

Figure 5 (a) XRD patterns of Ti–6Al–4V formed with a constant 8 mm tool diameter under varied step depths and feed rates. (b–d) Williamson–Hall plots for residual stress and crystallite size evaluation.

4. Results and Discussion

4.1 ISF XRD Patterns

The XRD patterns presented in Figure 4(a) demonstrate that while the primary α- phase reflections of Ti–6Al–4V remain stable under an unvarying tool diameter of 6 mm, changes in incremental step depth and feed rate lead to subtle peak broadening and shifts. Specifically, deeper step depths and slower feed rates promote increased peak broadness and minor shifts toward lower 2θ angles, indicative of elevated lattice strain and reduced crystallite size due to more severe plastic deformation. These observations align with findings by Muiruri et al. (2020), who reported that heat treatment-induced microstructural relaxation reduced defect density and lattice strain, thus significantly narrowing XRD peak width (Muiruri et al., 2020). Conversely, when step depths are shallow and feed rates are higher, the peaks are notably sharper, suggesting partial strain relief and retention of larger coherent domains.

The Williamson–Hall plots in Figures 4(b–d) quantify these effects: steeper negative slopes correspond to higher residual tensile strain and finer crystallite dimensions, while intercept values reflect inherent lattice distortion. Such methodology has been validated in prior studies as a reliable measure of microstructural refinement and residual stress (Nakamura et al., 2022). Together, the observed XRD trends and W–H analysis confirms that processing parameters in ISF serve as direct levers controlling the balance between structural strain and crystallite integrity, ultimately influencing the dimensional precision and mechanical robustness of formed Ti–6Al–4V components.

Figure 5(a) shows the XRD patterns of Ti–6Al–4V formed using a constant 8 mm tool diameter under different step depths and feed rates. The α-phase peaks remain dominant, indicating no phase transformation, but broader peaks and slight shifts toward lower 2θ values appear when using deeper step depths and lower feed rates. This suggests increased lattice strain and reduced crystallite size, consistent with previous findings in incremental forming studies (Oleksik et al., 2021) that reported higher strain accumulation with increased tool penetration depth.

The Williamson–Hall plots in Figures 5(b–d) quantify these effects, linking slope to crystallite size refinement and intercept to residual stress. As established in earlier research (Acevedo et al., 2023), this approach is a reliable method for evaluating microstructural changes, confirming that incremental forming parameters directly influence the microstrain–size balance, thereby affecting the mechanical performance and dimensional stability of Ti–6Al–4V components.

Figure 6(a) presents XRD patterns of Ti–6Al–4V formed with a constant 10 mm tool diameter, contrasting earlier results for 6 mm (Figure 4) and 8 mm (Figure 5) diameters. While all datasets preserve the α-phase peaks characteristic of HCP titanium, the 10 mm condition exhibits narrower peaks and reduced peak shifts, particularly at moderate step depths and feed rates. This indicates comparatively lower lattice strain and larger crystallite domains, suggesting that a larger tool radius can mitigate microstructural distortion during forming. Williamson–Hall plots in Figure 6(b–d) reinforce this interpretation: the slopes are less steep (indicating lower microstrain) and the intercepts are higher (suggesting larger D) than those for smaller tool diameters. Collectively, these results highlight that tool diameter is a key factor that modifies the influence of step depth and feed rate on residual stress and crystallite refinement critical for controlling dimensional stability and structural integrity in ISF processes.

4.2 Experimental Results, Modeling, and Optimization

The experimental results summarized in Table 5 provide valuable insight into the influence of process parameters tool radius (R), incremental step depth (S), and feed rate (F) on residual stress (RS) and crystallite size (D) in incremental forming of Ti–6Al–4V alloy. Across nine experimental runs, RS values ranged from −157.11 MPa to −86.99 MPa, indicating predominantly compressive stress states, whereas D varied between 19.67 nm and 21.87 nm. Statistical analysis resulted in two linear regression models, as presented in Equations (11) and (12).

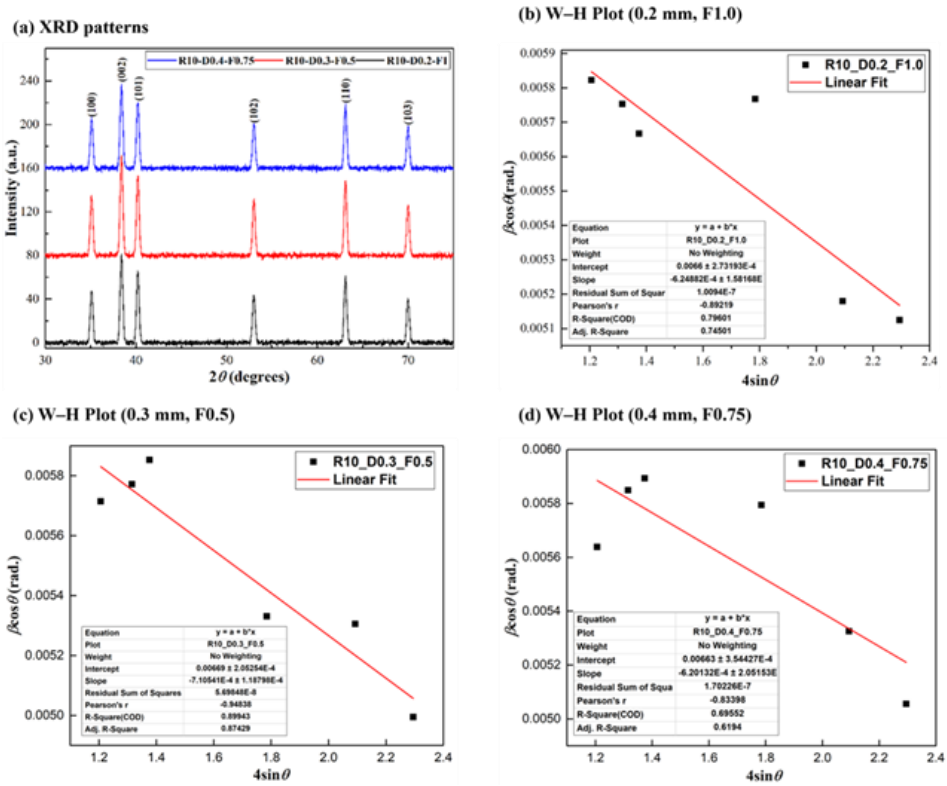

Figure 6 (a) XRD patterns of Ti–6Al–4V formed with a constant 10 mm tool diameter under varied step depths and feed rates. (b–d) Williamson–Hall plots for residual stress and crystallite size evaluation.

Table 5 Experimental runs and measured responses of residual stress (RS) and crystallite size (D) under different process parameter settings.

Run	Tool radius (mm)	Step depth (mm)	Feed rate (mm.min^{-1})	Residual stress, RS (MPa)	Crystallite size, D (nm)
1	6	0.2	0.5	−142.04	19.97
2	6	0.3	0.75	−127.48	20.45
3	6	0.4	1	−131.64	20.75
4	8	0.2	0.75	−157.11	19.67
5	8	0.3	1	−86.99	21.87
6	8	0.4	0.5	−103.09	21.38
7	10	0.2	1	−108.07	21.01
8	10	0.3	0.5	−122.89	20.73
9	10	0.4	0.75	−107.25	20.90

$$RS = -215.9756 + 5.2458(R) + 108.7333(S) + 27.5467(F) \quad (11)$$

$$D = 17.8028 + 0.1225(R) + 3.9667(S) + 1.0333(F) \quad (12)$$

These models reveal that incremental step depth exerts the largest effect on both RS and D, followed by feed rate, with tool radius having a smaller but still positive influence. A higher step depth reduces the magnitude of compressive RS (making RS less negative) and promotes an increase in crystallite size, likely due to reduced work hardening and altered thermal-mechanical conditions during deformation. This behavior is consistent with findings by Prasomthong & Onbat (2023), who observed that larger step depths in SPIF reduced residual stress concentration in aluminum alloys, and with Szpunar et al. (2024), who reported that process-induced thermal effects in Ti-based alloys influence grain coarsening and crystallite growth. From an industrial perspective, controlling step depth offers a

practical means of simultaneously moderating residual stress and tailoring crystallite size to improve dimensional stability and mechanical performance. This is particularly relevant for high- value applications such as aerospace and biomedical components, where surface integrity and microstructural precision are critical. By leveraging these regression models, manufacturers can optimize forming parameters for desired microstructural outcomes, thereby enhancing both product quality and process efficiency.

Table 6 presents a comparative evaluation of three predictive approaches Artificial Neural Network (ANN), linear regression, and the Taguchi method in estimating residual stress (RS) and crystallite size (D) for the given process parameters. The ANN model achieves exceptional prediction accuracy, with extremely low RMSE values (0.0301 MPa for RS and 0.1394 nm for D), coupled with minimal MAE and MAPE, indicating near- perfect agreement between predictions and actual measurements. In comparison, the regression and Taguchi models show considerably higher errors in RS prediction (RMSE of 15.2171 MPa and 11.6605 MPa, respectively), highlighting their limitations in capturing the nonlinear interactions between parameters that influence stress responses. While both methods perform reasonably for D prediction (RMSE under 0.46 nm for regression and 0. 26 nm for Taguchi), the substantial RS prediction errors reduce their suitability for precise residual stress control.

Overall, the ANN model demonstrates superior robustness and adaptability in modeling complex, nonlinear process– property relationships. Its implementation in process optimization can enable more accurate control of microstructural features and mechanical performance, thereby enhancing the consistency and quality of advanced manufacturing outcomes.

Table 7 summarizes the optimal process parameter settings derived from the integrated ANN–GA optimization approach. The optimal tool radius, step depth, and feed rate were found to be 8.725 mm**,** 0.2588 mm, and 1.00 mm.min^{-1}**,** respectively. Under these conditions, the predicted residual stress (RS) was −68.74 MPa, accompanied by a crystallite size (D) of 22.26 nm. This combination represents a balanced trade-off between minimizing residual stress and maximizing crystallite size, aligning with the dual-objective fitness function applied in the GA. The moderate tool radius likely provides sufficient heat generation and material flow, while the shallow step depth reduces excessive plastic deformation, thereby lowering tensile residual stress. The maximum feed rate further enhances thermal softening, contributing to reduced RS and a refined microstructure.

Table 6 Comparison of predicted residual stress (RS) and crystallite size (D) values obtained from ANN, regression, and Taguchi models, along with associated error metrics (RMSE, MAE, and MAPE).

Run	Pre.ANN (RS)	Pre.ANN (D)	Pre.Regression (RS)	Pre.Regression (D)	Pre.Taguchi (RS)	Pre.Taguchi (D)
1	−142.040	19.995	−148.981	19.848	−150.676	19.804
2	−127.538	20.626	−131.221	20.503	−135.329	20.251
3	−131.610	20.620	−113.461	21.158	−115.156	21.114
4	−157.094	19.600	−131.603	20.351	−140.626	20.034
5	−86.980	21.788	−113.843	21.006	−95.625	21.704
6	−103.105	21.357	−116.743	20.886	−110.939	21.181
7	−108.104	20.947	−114.224	20.854	−115.919	20.811
8	−122.846	20.628	−117.124	20.734	−106.406	21.094
9	−107.236	21.216	−99.364	21.389	−115.886	20.734
RMSE	0.0301	0.1394	15.2171	0.4597	11.6605	0.2580
MAE	0.0246	0.1097	12.7422	0.3634	10.9896	0.2430
MAPE (%)	0.0205	0.5283	11.0798	1.7401	9.0578	1.1774

Table 7 Optimal process parameters and corresponding predicted responses obtained from the ANN-GA optimization approach

Tool_Radius (mm)	Step_Depth (mm)	Feed_Rate (mm.min^{-1})	Residual Stress (RS)	Crystallite Size (D)
8.725	0.2588	1.00	−68.74	22.26

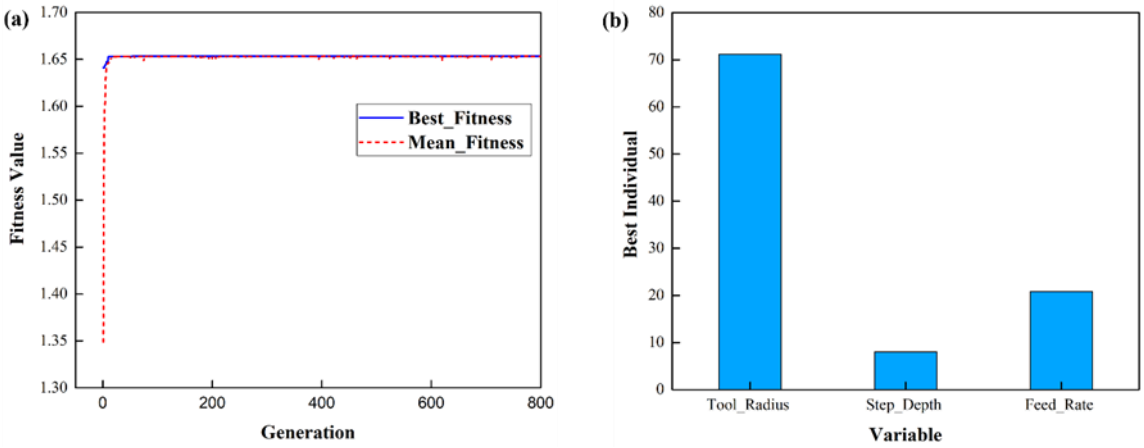

Figure 7 Genetic algorithm optimization performance: (a) Convergence trends of best and mean fitness values over generations and (b) relative contribution of process variables to the optimal solution.

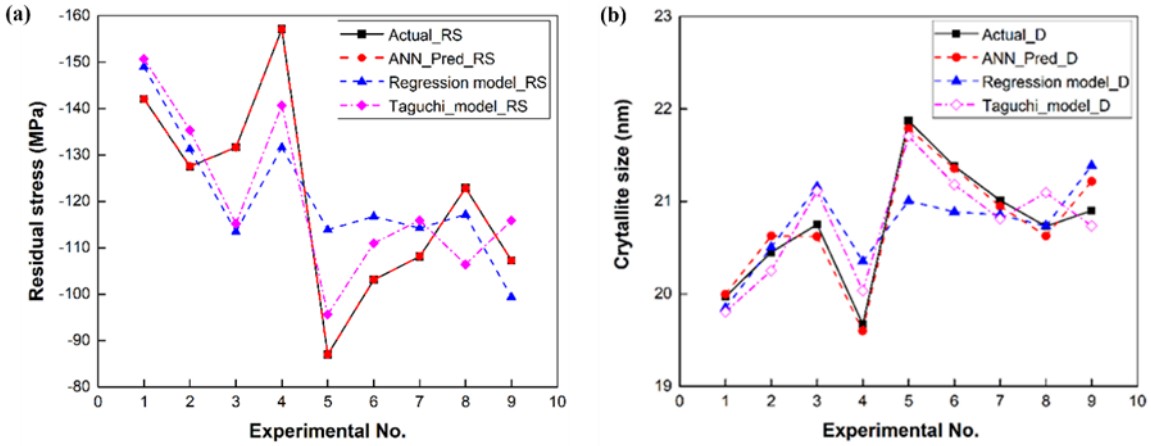

Figure 8 Comparison between experimental and predicted values of (a) residual stress and (b) crystallite size obtained from the ANN, regression, and Taguchi models

These results confirm the ANN– GA framework's capability to efficiently navigate complex, nonlinear process– response relationships and identify parameter sets that simultaneously improve multiple microstructural performance indicators. In practical terms, this optimal configuration could enhance the dimensional stability and fatigue resistance of the processed material while maintaining a fine-grained structure advantageous for mechanical properties

Figure 7 illustrates the outcomes of the GA-based optimization process for predicting residual stress (RS) and crystallite size (D). In Figure 7(a), the convergence curve shows that the *best fitness* rapidly increased during the initial ~50 generations before stabilizing around 1. 65, indicating that the optimal solution was found early and maintained across 800 generations. The *mean fitness* followed a similar trend, converging close to the best fitness value, which reflects high population consistency and the absence of premature convergence. In Figure 7(b), the relative contribution analysis reveals that tool radius was the most influential parameter (≈72% contribution) in achieving the optimal responses, followed by feed rate (≈21%) and step depth (≈7%). This suggests that adjusting tool radius has the greatest potential for controlling RS and D in this process, consistent with prior studies reporting its strong effect on heat input and microstructural evolution in friction stir– type processes.

In this study, the predictive capability of the Artificial Neural Network (ANN) model was evaluated against conventional regression and Taguchi- based

approaches for estimating residual stress (RS) and crystallite size (D) in the incremental forming process. As illustrated in Figure 8(a), the ANN model demonstrated an exceptional ability to follow the experimental RS trend across all nine runs, with minimal deviation from the actual measurements. This was particularly evident in high-magnitude compressive stress regions (e.g., Runs 1–3 and 6–8), where the regression and Taguchi models exhibited noticeable under- or over-estimation. The superior accuracy of the ANN is quantitatively supported by the error metrics in Table 6**,** where ANN achieved the lowest RMSE, MAE, and MAPE values for both RS and D, underscoring its robustness in capturing the nonlinear relationships between process parameters and mechanical responses.

Similarly, Figure 8(b) shows that for crystallite size predictions, all three models provided relatively close estimates to the experimental data, but the ANN consistently achieved the closest match, with prediction curves nearly overlapping the actual measurements in most runs. This advantage is attributed to the ANN's capacity for nonlinear mapping and complex pattern recognition, enabling it to account for subtle interactions between tool radius, incremental step depth, and feed rate that linear regression or fixed-level Taguchi models cannot fully capture. Overall, the combined graphical and statistical evidence confirms that the ANN model significantly outperforms regression and Taguchi methods in both accuracy and generalization capability. This positions ANN as a powerful and reliable tool for process modeling and optimization in advanced manufacturing applications, where high prediction fidelity is critical for determining optimal parameter settings and ensuring targeted microstructural and mechanical outcomes.

4.3 Discussion

The combined ANN–GA framework demonstrates superior capability in simultaneously controlling residual stress (RS) and crystallite size (D) during incremental forming of Ti–6Al–4V. The ANN model achieved high predictive accuracy, with training RMSE values of 0.0301 MPa for RS and 0.1394 nm for D (Table 6), while validation RMSE values of 1.842 MPa and 0.229 nm, respectively, confirm good generalization. These results indicate that the ANN effectively captures the nonlinear relationships among tool radius, step depth, and feed rate, outperforming regression and Taguchi methods, consistent with previous studies (Kumar et al., 2021; Costa et al., 2022). The GA optimization identified optimal parameters (R = 8.725 mm, S = 0.2588 mm, F = 1.00 mm·min^{-1}), yielding a residual stress of −68.74 MPa and a crystallite size of 22.26 nm, thereby achieving a balance between distortion reduction and microstructural control. This agrees with prior findings highlighting the influence of process parameters on stress evolution and microstructure (Maqbool et al., 2019; Liao et al., 2025). Moreover, the ANN–GA integration aligns with materials-by-design approaches for tailoring mechanical performance (Shang et al., 2023). Based on the optimization and XRD analysis, practical guidelines for ISF of Ti–6Al–4V are proposed. Specifically, shallow step depths (<0.30 mm) and moderate tool radii (8–10 mm) reduce lattice distortion while maintaining stable material flow, whereas higher feed rates promote thermal softening and reduce residual stress. These findings provide effective parameter-selection criteria for controlling surface integrity, residual stress distribution, and crystallite size in industrial ISF applications.

Indeed, our results reinforce the broader relevance of residual stress management in additive and subtractive processes. Residual stress critically affects distortion and part reliability (Bastola et al., 2023), and has been a persistent challenge in machining and forming of Ti alloys (Zou et al., 2024). Advanced hybrid modeling methodologies such as coupling thermal analysis with GA-driven optimization have shown promise in mitigating these effects (Chen et al., 2023). In SPIF and two-point incremental forming (TPIF), targeted residual stress manipulation via process parameter tuning has been validated as a means of enhancing fatigue life and geometric accuracy (Maqbool et al., 2021; Maqbool et al., 2019).

Finally, the proposed ANN–GA framework aligns with the industrial drive toward smart manufacturing and digital twin strategies, where predictive, coupled models are essential for real-time process adaptation (Shang et al., 2023). By enabling high-fidelity optimization of forming parameters, our methodology not only improves part integrity and surface quality but also provides a practical foundation for future work that integrates in-situ monitoring and adaptive control, as envisioned in recent studies across the industry 4.0 domain (Radu et al., 2013; Bastola et al., 2023).

For future work, the developed ANN–GA framework may be extended to other difficult-to-form materials such as Inconel alloys, β-titanium grades, or

magnesium alloys. Since their deformation mechanisms differ significantly from Ti– 6Al– 4V, additional calibration of diffraction elastic constants and peak-selection criteria will be required to achieve accurate residual-stress prediction and microstructural optimization.

5. Conclusion

This work demonstrates an effective ANN–GA approach for optimizing incremental sheet forming of Ti– 6Al– 4V. The model accurately predicted the influence of tool radius, step depth, and feed rate on residual stress and crystallite size, achieving superior performance compared with regression and Taguchi methods. The optimized parameters (R = 8.725 mm, S = 0.2588 mm, F = 1.00 mm.min^{-1}) were experimentally validated, confirming the framework's ability to guide microstructural control. Limitations include the use of a single sheet thickness and room-temperature forming; future studies should consider thermal assistance, multi-material validation, and in-situ monitoring.

6. Abbreviations

Abbreviation	Full Term
ANN	Artificial Neural Network
GA	Genetic Algorithm
ANN–GA	Artificial Neural Network–Genetic Algorithm
ISF	Incremental Sheet Forming
SPIF	Single-Point Incremental Forming
TPIF	Two-Point Incremental Forming
RS	Residual Stress
D	Crystallite Size
R	Tool Radius
S	Incremental Step Depth
F	Feed Rate
XRD	X-ray Diffraction
W–H	Williamson–Hall
UDSM	Uniform Deformation Stress Model
FWHM	Full Width at Half Maximum
HCP	Hexagonal Close-Packed
BCC	Body-Centered Cubic
RMSE	Root Mean Squared Error
MAE	Mean Absolute Error
MAPE	Mean Absolute Percentage Error
R^2	Coefficient of Determination

7. Acknowledgements

The authors would like to express their sincere appreciation to the Faculty of Industrial Technology and the Faculty of Engineering at Nakhon Phanom University, the Faculty of Engineering at Khon Kaen University, and the Faculty of Industrial Technology at Sakon Nakhon Rajabhat University for their generous support and for providing access to the necessary testing laboratories. Their technical assistance and institutional support played a vital role in the successful completion of this research.

8. CRediT Statement

Apisit Keawchalun: Conceptualization, methodology, software, formal analysis, data curation, laboratory experiments, visualization, writing – original draft, writing – review & editing.
Suriya Prasomthong: Laboratory experiments, software, visualization, data curation, formal analysis, writing – review & editing.
Thanatep Phatungthane: Validation, writing – review & editing, supervision.
Chaiya Chomchalao: Conceptualization, resources, supervision, project administration, writing – review & editing, funding acquisition.

9. References

Acevedo, R. B., Kantarowska, K., Santos, E. C., & Fredel, M. C. (2023). Residual stress measurement techniques for Ti6Al4V parts fabricated using selective laser melting: State of the art review. *Rapid Prototyping Journal*, *29*(8), 1549-1564. https://doi.org/10.1108/RPJ-04-2019-0097

Bastola, N., Jahan, M. P., Rangasamy, N., & Rakurty, C. S. (2023). A review of the residual stress generation in metal additive manufacturing: Analysis of cause, measurement, effects, and prevention. *Micromachines*, *14*(7), Article 1480. https://doi.org/10.3390/mi14071480

Charonerat, S., Phatungthane, T., & Summatta, C. (2025). Optimizing friction stir welding parameters for enhanced mechanical properties of dissimilar aluminum alloys AA5083 and AA6063: A Taguchi approach. *International Journal of Applied Science and Engineering, 22*(3), 1–10. https://doi.org/10.6703/IJASE.202509_22(3).006

Chen, X., Xie, X., Wu, H., Ji, X., Shen, H., Xue, M., ... & Liu, Q. (2023). In-situ control of residual stress and its distribution in a titanium alloy

additively manufactured by laser powder bed fusion. *Materials Characterization*, *201*, Article 112953. https://doi.org/10.1016/j.matchar.2023.112953

Coman, C. C., Mazurchevici, S. N., Carausu, C., & Nedelcu, D. (2023). Analysis of incremental sheet forming of aluminum alloy. *Materials*, *16*(19), Article 6371. https://doi.org/10.3390/ma16196371

Costa, A., Buffa, G., Palmeri, D., Pollara, G., & Fratini, L. (2022). Hybrid prediction-optimization approaches for maximizing parts density in SLM of Ti6Al4V titanium alloy. *Journal of Intelligent Manufacturing*, *33*(7), 1967-1989. https://doi.org/10.1007/s10845-022-01938-9

Kajal, G., Tyagi, M. R., & Kumar, G. (2023). A review on the effect of residual stresses in incremental sheet metal forming used in automotive and medical sectors. *Materials Today: Proceedings*, *78*(3), 524-534. https://doi.org/10.1016/j.matpr.2022.11.235

Kumar, P., Karsh, P. K., Misra, J. P., & Kumar, J. (2021). Multi-objective optimization of machining parameters during green machining of aerospace grade titanium alloy using Grey–Taguchi approach. *Proceedings of the Institution of Mechanical Engineers, Part E: Journal of Process Mechanical Engineering*, *235*(1), 93–106. https://doi.org/10.1177/09544089211043610

Kumar, R., Kumar, G., & Singh, A. (2020). An assessment of residual stresses and micro-structure during single point incremental forming of commercially pure titanium used in biomedical applications. *Materials Today: Proceedings*, *28*(2), 1261-1266. https://doi.org/10.1016/j.matpr.2020.04.147

Liao, J., Huang, Y., Lu, X., Jiang, Y., & Hussain, G. (2025). Hybrid incremental forming processes: a review. *The International Journal of Advanced Manufacturing Technology*, *136*(7), 3077-3109. https://doi.org/10.1007/s00170-025-15075-z

Maqbool, F., & Bambach, M. (2019). Experimental and numerical investigation of the influence of process parameters in incremental sheet metal forming on residual stresses. *Journal of Manufacturing and Materials Processing*, *3*(2), Article 31. https://doi.org/10.3390/jmmp3020031

Maqbool, F., Maaß, F., Buhl, J., Hahn, M., Hajavifard, R., Walther, F., ... & Bambach, M. (2021). Targeted residual stress generation in single and two point incremental sheet forming (ISF). *Archive of Applied Mechanics*, *91*(8), 3465-3487. https://doi.org/10.1007/s00419-021-01935-z

Nakamura, K., Kawaguchi, T., Ikeda, H., Karntiang, P., Kakura, K., Taniguchi, Y., Toyoda, K., Shimizu, H., & Kido, H. (2022). Bond durability and surface states of titanium, Ti-6Al-4V alloy, and zirconia for implant materials. *Journal of Prosthodontic Research, 66*(2), 296–302. https://doi.org/10.2186/jpr.JPR_D_20_00297

Muiruri, A., Maringa, M., & Du Preez, W. (2020). Evaluation of dislocation densities in various microstructures of additively manufactured Ti6Al4V (ELI) by the method of x-ray diffraction. *Materials*, *13*(23), Article 5355. https://doi.org/10.3390/ma13235355

Murugesan, M., Yu, J. H., Jung, K. S., Cho, S. M., Bhandari, K. S., & Lee, C. W. (2022). Optimization of forming parameters in incremental sheet forming of AA3003-H18 sheets using Taguchi method. *Materials*, *15*(4), Article 1458. https://doi.org/10.3390/ma15041458

Oleksik, V., Trzepieciński, T., Szpunar, M., Chodoła, Ł., Ficek, D., & Szczęsny, I. (2021). Single-point incremental forming of titanium and titanium alloy sheets. *Materials*, *14*(21), Article 6372. https://doi.org/10.3390/ma14216372

Ortiz, M., Penalva, M., Iriondo, E., & Lopez de Lacalle, L. N. (2019). Accuracy and surface quality improvements in the manufacturing of Ti-6Al-4V parts using hot single point incremental forming. *Metals*, *9*(6), Article 697. https://doi.org/10.3390/met9060697

Popp, G. P., Racz, S. G., Breaz, R. E., Oleksik, V. Ș., Popp, M. O., Morar, D. E., ... & Popp, I. O. (2024). State of the art in incremental forming: Process variants, tooling, industrial applications for complex part manufacturing and sustainability of the process. *Materials*, *17*(23), Article 5811. https://doi.org/10.3390/ma17235811

Prasomthong, S., & Onbat, K. (2023). The Optimization of sheet forming on residual stress and surface roughness with two point incremental forming process (TPIF) of

aluminum alloy parts. *Applied Science and Engineering Progress*, *16*(4), 6059-6059. https://doi.org/10.14416/j.asep.2022.06.003

Radu, C., Tampu, C., Cristea, I., & Chirita, B. (2013). The effect of residual stresses on the accuracy of parts processed by SPIF. *Materials and Manufacturing Processes*, *28*(5), 572-576. https://doi.org/10.1080/10426914.2013.763967

Shang, X., Liu, Z., Zhang, J., Lyu, T., & Zou, Y. (2023). Tailoring the mechanical properties of 3D microstructures: A deep learning and genetic algorithm inverse optimization framework. *Materials Today*, *70*, 71-81. https://doi.org/10.1016/j.mattod.2023.09.007

Szpunar, M., Trzepieciński, T., Ostrowski, R., Żaba, K., Ziaja, W., & Motyka, M. (2024). Thermo-mechanical numerical simulation of friction stir rotation-assisted single point incremental forming of commercially pure titanium sheets. *Materials*, *17*(13), Article 3095. https://doi.org/10.3390/ma17133095

Zou, Z., Zhang, T., He, L., Zhao, X., & Zhou, T. (2024). Hybrid modeling prediction of residual stresses in turned Ti6Al4V considering frictional contact. *Journal of Materials Research and Technology*, *30*, 4377-4392. https://doi.org/10.1016/j.jmrt.2024.04.157